scientific reports

Check for updates

OPEN

The role of SiO_2 buffer layer in the molecular beam epitaxy growth of $CsPbBr_3$ perovskite on Si(111)

Paola De Padova[1]✉, Carlo Ottaviani[1], Bruno Olivieri[2], Yurii P. Ivanov[3], Giorgio Divitini[3]✉ & Aldo Di Carlo[1]✉

Here we present the growth of molecular beam epitaxy (MBE) $CsPbBr_3$ perovskite films in the orthorhombic crystal structure, with unique structural and morphological properties. $CsPbBr_3$ MBE perovskite films, with thickness ranging from a few nm to 300 nm, were grown in ultra-high vacuum on a Si(111)7 × 7 reconstructed surface, and after the formation of about 2 nm of SiO_2, obtained exposing the clean reconstructed Si surface to molecular oxygen that serves to decouple the film from substrate. X-ray diffraction, and electron microscopies, such as scanning electron microscopy and high-angle annular dark-field scanning transmission electron microscopy measurements showed remarkable structural, as well as morphological features, indicating extremely high crystallinity over a large area and across the bulk of the perovskite film. Through the X-ray diffraction patterns we found very narrow (002) and (110) reflections of $CsPbBr_3$ in pure orthorhombic phase, exhibiting a full width at half maximum of only 0.035°, value similar to a bulk Si single crystals, and a surface morphology composed of flat areas up to micrometres in lateral size. Our results shed new light both on preparation of high crystal quality perovskite films, and on the intrinsic properties of this striking fully-inorganic materials, which are exploitable for potential applications in electronic/optoelectronic devices and next generation photovoltaic solar cells.

The term perovskite describes a wide class of compounds having a crystal structure similar to the $CaTiO_3$[1–4], where the unit cell generally consists of a Ti atom coordinated with six O atoms to form a TiO_6 octahedron, and slightly rotated TiO_6 octahedra are connected at a vertex to form a three-dimensional networked structure[5,6].

Beside oxide perovskites, the halide perovskite gained the attention of the scientific community after 2009, when Kojima and collaborators published their seminal work on photovoltaic (PV) cells, based on hybrid halide organic–inorganic perovskite[7]. In fact, organometal halide perovskites $CH_3NH_3PbBr_3$ and $CH_3NH_3PbI_3$ (where $CH_3NH_3^+$ and Pb^{2+} are the metallic cations, and I^- and Br^-, and Cl^- the non-metal anions) were used as visible-light sensitizers for these two first prototypal PV devices, exhibiting a power conversion efficiency of 3.13 (%) and 3.81 (%), respectively[7]. This opened a path for an intense worldwide scientific push, leading towards the development of countless, and very varied optoelectronic and PV perovskite-based applications[8,9]. Furthermore, a large number of different elements and compounds can be combined to form a perovskite structure, and using this compositional flexibility, scientists aim to design perovskite crystals that exhibit different physical, optical, and electrical characteristics[9].

Currently, all-inorganic caesium lead halide perovskites, $CsPbX_3$[10–13], represent a very important class of compounds, particularly due to their increased stability and carriers conductivity compared to their hybrid organic–inorganic counterparts[14]. Therefore, the enhanced thermal and chemical stability observed in fully-inorganic $CsPbBr_3$ perovskite layers with respect to hybrid perovskites, posed challenges in both synthesis and investigation of their physical and chemical properties. The greater stability is very relevant for potential technological applications, also owing to the significantly elevated decomposition temperature of $CsPbBr_3$, approximately 577 °C[15,16].

[1]National Research Council, Institute of Structure of Matter (CNR - ISM), Via Fosso del Cavaliere, 100, 00133 Roma, Italy. [2]National Research Council, Institute of Atmospheric Sciences and Climate (CNR - ISAC), Via Fosso del Cavaliere, 100, 00133 Roma, Italy. [3]Electron Spectroscopy and Nanoscopy, Italian Institute of Technology (IIT), Via Morego, 30, 16163 Genova, Italy. ✉email: depadova@ism.cnr.it; Giorgio.Divitini@iit.it; aldo.dicarlo@ism.cnr.it

In $CaTiO_3$[5], the rotation of TiO_6 octahedra and the relative displacement of the cations reduces the crystal symmetry to the orthorhombic or tetragonal. Similarly, the ideal cubic $Pm\ \bar{3}\ m$ structure[5,6] of the $CsPbBr_3$ perovskite can be modified into two different structural phases, including, the tetragonal *P4/mbm*, and the orthorhombic *Pbnm*, in which the Pb atom is located in the centre of the octahedra formed by six Br atoms, whereas the Cs atoms are located in the three-dimensional framework cavities. At room temperature (RT) the $CsPbBr_3$ perovskite is monoclinic distorted[17]. It crystallizes in the orthorhombic (*Pnma*) phase, adopting the distorted perovskite structure, with $a = 8.2440(6)$ Å, $b = 8.1982(8)$, and $c = 11.7351(11)$ Å, as determined by the single-crystal diffraction[18]. The $\{PbBr_6\}^{4-}$ octahedra are tilted with respect to the orthogonal geometry of the ideal cubic perovskite structure[17]. Two successive temperature phase transitions of orthorhombic $CsPbBr_3$ occur at 88 °C and 130 °C, transforming the crystal structure to tetragonal (*P4/mbm*) and cubic (*Pm-3 m*), respectively[18], as already observed by x-ray analysis and neutron diffraction, by Moller et al.[17], and Hirotsu et al.[19], as second and first order phase transitions, respectively.

A wide range of synthesis techniques have been applied to produce full-inorganic $CsPbBr_3$ single crystal perovskites. For example, a vertical two-zone tube furnace using an electronic dynamic gradient method showed relevant structural and optical properties, exhibiting extremely high crystalline quality[20]. On the other hand, colloidal $CsPbBr_3$ perovskite quantum dots with orthorhombic structure (*Pnma*) were successfully prepared[21], and catalyst-free, solution-phase synthesis of $CsPbX_3$ (X = Br, I) nanowires was reported[22]. Furthermore, monodisperse colloidal nanocubes (from 4 to 15 nm edge lengths) of fully inorganic caesium lead halide perovskites ($CsPbX_3$, X = Cl, Br, and I or mixed halide systems Cl/Br and Br/I), showing nanocrystals with cubic shape and cubic perovskite crystal structure[23], and also colloidal $CsPbBr_3$ perovskite nanocrystals, with orthorhombic phase, exhibiting luminescence beyond traditional quantum dots[24], were synthesised. Techniques such as physical and chemical vapor depositions for these materials have recently emerged, with the potential to enable a perovskite active layer in a device that can be more stable against exposure to air, mainly due to reduced moisture permeability and/or crystalline structure, as well as morphology modifications[25,26]. A comprehensive review on the state of the art and outlooks on halide perovskite nanocrystals has been recently reported by Dey et al.[27], taking into account of the main outstanding physics/chemistry and device engineering achievements.

Vapour physical deposition methods embrace molecular beam epitaxy, thermal deposition, chemical vapour deposition, as well as plasma sputtering, and UHV-MBE considered the main technique for epitaxial deposition. Epitaxial and quasiepitaxial growth of halide perovskites represent the edges for succeeding new materials, with a better control over the film structures and quality, as well as low level of defects suitable for high end optoelectronics[28].

Remarkably, epitaxial growth of cubic phase of $CsPbBr_3$ has been demonstrated on a metal oxide perovskite $SrTiO_3(100)$ substrate, via pulsed laser deposition (PLD)[29], and chemical vapor-phase deposition (CVD), at a reaction temperature of 450 °C[30]. In both cases[29,30], films of high crystal quality were obtained, exhibiting a photoluminescence (PL) peak at 525 nm with a full width at half maximum (FWHM) of just 19 nm[29], and a (100) X-ray diffraction (XRD) reflection wide of only 0.18° (FWHM)[30]. In 2023, fully inorganic $CsPbBr_3$ films, exhibiting large columnar grains, with different sizes up to ~ 7 μm , and a preferential (001) crystal orientation, were grown at a base pressure of about 2.7×10^{-5} mbar, by thermal vapour deposition and subsequently annealing at high temperature of 375 °C[31]. In addition, molecular beam epitaxy (MBE) was used to synthetize both $CsPbBr_3$ and $CsSnBr_3$ on an Au(001) single crystal[32]. While these results are extremely valuable, in order to enable applications in real-world devices it is essential to expand the group of potential substrates, particularly including technologically-relevant materials such as silicon and other conventional device components.

In this work, we report for the first time, $CsPbBr_3$ films grown in a wide thickness range (from 10 to 300 nm) on $Si(111)7 \times 7$ by ultra-high vacuum (UHV) molecular beam epitaxy (MBE). Thin perovskite film exhibited a $\times 2$ reconstruction on $Si(111)7 \times 7$, whereas, for the thicker one the interaction with substrate was mediated by a very thin amorphous layer of SiO_2, obtained by exposing the clean $Si(111)7 \times 7$ reconstructed surface to pure O_2, at room temperature (RT). The presence of the thin SiO_2 on the Si substrate permits the growth of highly ordered orthorhombic phase of thick $CsPbBr_3$ (300 nm) film, exhibiting unique structural and morphological, properties, as probed by X-ray diffraction, scanning electron microscopy (SEM), as well as high-angle annular dark-field scanning transmission electron microscopy (HAADF STEM). The thin layer of SiO_2 acted as a cushion layer to promote the MBE growth of very thick perovskite, decoupling the otherwise highly mismatched film from the silicon substrate.

Results and discussion

The $CsPbBr_3$ powder, to be used as precursor for MBE growth inside a UHV-MBE Knudsen cell, was first characterised. The X-ray diffraction pattern of such powder displayed orthorhombic symmetry (*Pbnm* (62) space group)[15,18,20,33–35] (Supplementary Fig. S1). This is in agreement with the orthorhombic symmetry, for which Rietveld refinement measurements have been recently reported in the literature both through high-resolution (HR) synchrotron XRD at ALBA (Spain) facility[35], and neutron powder diffraction SINQ spallation source, at PSI (Switzerland)[35] on $CsPbBr_3$ perovskite, and already applied to nanowires[34], nanotwins[36], nanodots[21], as well as nanocrystal superlattices[37]. In particular, a clear splitting of the (110) and (220) peaks in the diffraction pattern was observed[20]. Moreover, in our measurements we do not find evidence of the presence of an additional $PbBr_2$ phase originating from perovskite decomposition, typically found with XRD peaks at 14.37°, 18.58°, 21.63°, 22.04° and 23.69°, which correspond to the lattice planes (101), (002), (011), (102) and (111)[38]. This proves the high purity of the $CsPbBr_3$ powder used for our UHV MBE film growths.

The samples were grown in a base pressure of 8.0×10^{-10} mbar in a Knudsen evaporation cell with a rate of ~ 0.1 Å/s, keeping the substrates at temperature of ~ 130 °C.

A preferential growth orientation of $CsPbBr_3$ (*Pnma* space group, with $a = 8.2440$ Å, $b = 8.1982$, $c = 11.7351$ Å), on Si(111)7 × 7 (space group $Fd\bar{3}m$, with $a_{Si} = b = c = 5.43$ Å) is obtained, assuming a large lattice mismatch factor of 7% [$f = (1 - a_{overlayer}/a_{substrate})$], for the planes $(001)_{CsPbBr3}$ being parallel to $(111)_{Si}$ with the lattice constant $a_{CsPbBr3}$ much higher than a_{Si}. Despite such a large difference in lattice constants, one-unit cell of $CsPbBr_3$, along the [1–10]Si direction, could match with two-unit cells of Si in a × 2, as shown on the RHEED pattern (Fig. 1). The RHEED pattern, collected with the direction of electron beam parallel to the [11–2]Si, of the Si(111)7 × 7 surface (Fig. 1a), and a deposited thin film of $CsPbBr_3$ (Fig. 1b), show the streaks (− 1/7, 1/7) of the clean Si(111)7 × 7 surface before the growth, and (− 1/2,1/2) spots, induced by the film growth. The poor sharpness and spot-like appearance of the streaks (− 1/2,1/2) of the $CsPbBr_3$ film indicate the coalescence of $CsPbBr_3$ islands during the growth.

It is worth noting that the preferential growth mode of $CsPbBr_3$ perovskite directly on reconstructed Si(111)7 × 7 is quite promising, but the film develops from the beginning more appropriately as island-like, Volmer-Weber mode, and/or as Stranski–Krastanov growth mode[39,40], rather than as a needed continuous film.

To improve the crystal quality of the $CsPbBr_3$ film, we designed a structure with a buffer layer between the film and the Si(111)7 × 7 surface. For this we chose SiO_2, for which *in-situ* Auger Electron Spectroscopy spectra are shown (Supplementary Fig. S2). The formation of an amorphous SiO_2 layer on the Si(111)7 × 7 surface is a simple and straightforward process. Furthermore, this is expected to be relevant for technological applications: in optoelectronic systems, active perovskite is frequently deposited on oxide layers[12,13,29–31]. The main idea behind this architecture is to decouple the surface atoms of the Si substrate from the perovskite film via a very thin amorphous SiO_2 buffer layer, to minimise constraints on nucleation and favour epitaxial growth from the initial, seeding perovskite layer. This is facilitated by the intact arrival of the entire $CsPbBr_3$ molecule on the substrate surface, as confirmed by mass spectrometry (Supplementary Fig. S3), enabling the $CsPbBr_3$ molecules to self-organize based on the optimized temperature applied to the Si substrate and the molecular flux from the MBE cell.

Various $CsPbBr_3$ films have been grown, by considering different substrate's temperatures, from RT up to 250 °C, and with different Knudsen cell fluxes, from 0.1 up to 18 Å/s, to find optimal conditions for continuous growth of large-scale epitaxial films, trying to keep the same thickness of the films, as measured by a quartz microbalance.

The thickness of the films, as measured by a quartz microbalance, was kept constant. Using *ex-situ* analysis by XRD, EDS, SEM, and HAADF STEM, as well as differential phase contrast (DPC) STEM we find that the optimal conditions are $T_{substrate} = 130$ °C and cell flux of ~ 0.1 ÷ 0.2 Å/s .

The XRD pattern from a 300 nm-thick $CsPbBr_3$ film grown on SiO_2/Si(111)7 × 7 at 130 °C is shown (Fig. 2a). This pattern features a very intense peak at 15.195°, and two other peaks at 30.700°, and 28.435°, where the first two are associated with orthorhombic $CsPbBr_3$ perovskite, and the latter is the (111) reflection from the substrate. The detailed structure of the perovskite peaks at 2ϑ of 15.2° and 30.7°, is reported (Fig. 2b and c).

The XRD peaks for the $CsPbBr_3$ film are not fully symmetric, due to the presence of multiple contributions. To get clearer physical insights and attribute each contribution of the X-ray diffraction peaks, signing, noteworthy for the first time, a limit of their FWHM, a least-square fitting procedure, using the convolution of Gaussian and Lorentzian functions, has been applied to isolate these components, findings four components for both peaks. In fact, we have to consider that each XRD peak contains two reflections, the (002) (110), (004) and (220) of orthorhombic $CsPbBr_3$ phase. Additionally, the X-ray beam consists of two photon lines, Cu $K\alpha_1$ and Cu $K\alpha_2$, as the X-ray source is not monochromatic. The first two peaks at lower angles (pink and blue lines of Fig. 2b) are located at 15.187° ± 0.02°and 15.203° ± 0.02°, while the first two peaks at higher angles (pink and blue lines of Fig. 2c) are located at 30.688° ± 0.02°and 30.704° ± 0.02°. These components are attributed to (002) (110) and (004) (220) reflections of the orthorhombic $CsPbBr_3$ perovskite phase (*Pnma* (62) space group), in good agreement with

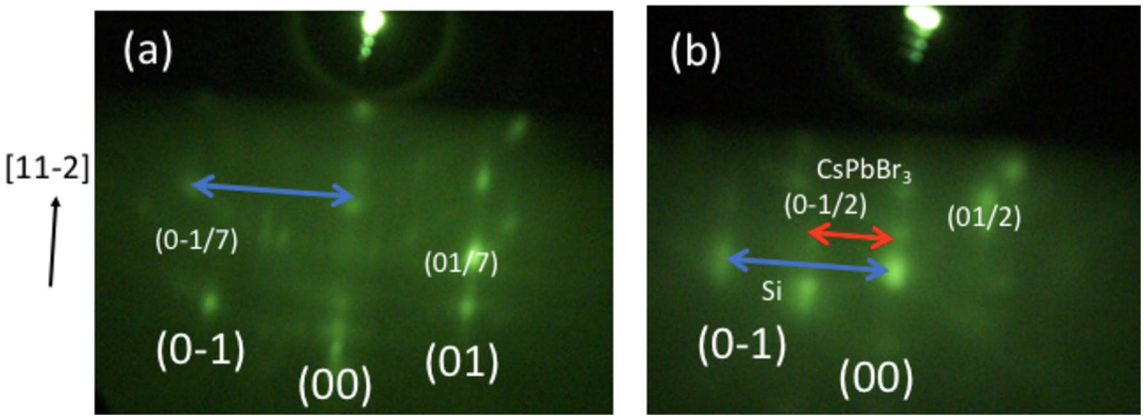

Figure 1. RHEED patterns collected on clean Si(111)7 × 7 (**a**), and after the deposition of ~ 100 Å of $CsPbBr_3$, (**b**). The arrows indicate the bulk Si (blue) integer streaks order (00), (0–1), (01), and the fractional streaks order of the × 2 $CsPbBr_3$ film (red), in reciprocal space; the primary energy (Ep) is 12 keV; the Ep incident beam was parallel to the [11–2] orientation of Si(111), while the fractional streaks order (0–1/7), and (01/7), stemming from the × 7 Si reconstruction are marked.

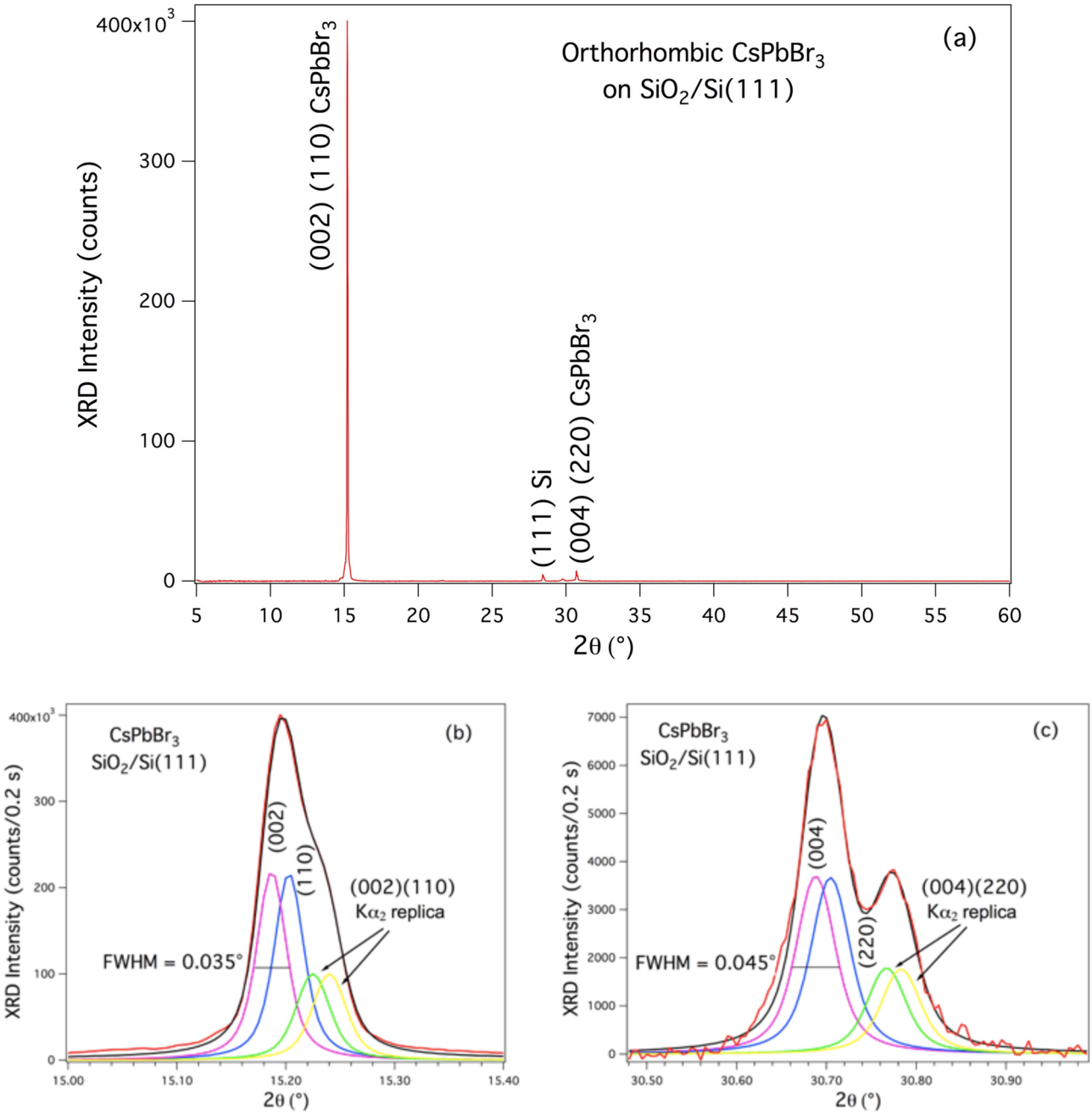

Figure 2. XRD from $CsPbBr_3$ films grown on thin SiO_2/Si (111)7 × 7 at substrate temperature of 130 °C (**a**); (**b**) and (**c**) are the enlarged regions around 2θ of 15° and 30° of the profile (**a**). The least-square fitting procedure, by using the convolution of Gaussian and Lorentzian functions, employing four components for each peak are reported (pink, blue, green and yellow lines), identifying the main (002)/(004) and (110)/(220) components as due to the orthorhombic $CsPbBr_3$ structure, and the others (green and yellow line) as their Cu $K\alpha_2$ X-ray replica.

literature[15,18,20,21,33–37]. The other lines (green and yellow curves) with peaks at 15.225° ± 0.02°, and 15.240° ± 0.02°, (Fig. 2b) and 30.767° ± 0.02°, and 30.783° ± 0.02°, (Fig. 2c), are peak replica originating from the Cu $K\alpha_2$ X-ray (λ = 1.54439 Å). According to the Bragg's law, the spacing between the two lines, Cu $K\alpha_1$, and Cu $K\alpha_2$, split by a given energy interval, increases with the 2θ diffraction angle value, producing that the replica at higher 2θ angle (Fig. 2c) are better separated, from their main peaks, while are just a shoulder at lower angle (Fig. 2b). The intensity of each component have been fitted, under the constrain that the replica of the Cu $K\alpha_2$ x-ray line have a natural half intensity with respect to the main Cu $K\alpha_1$ X-ray line (λ = 1.54056 Å), and, furthermore, their angle positions imposed by the Cu $K\alpha_2$ wavelength. It is worth noting that, for the four components of each peak similar parameters were used: (Gaussian width, σ_G, and Lorentzian width, Γ_L) $\sigma^{(002),\,(110)}{}_G = 0.020°$;$\Gamma^{(002),\,(110)}{}_L = 0.020°$; $\sigma^{\text{replica }(002),\,(110)}{}_G = 0.025°$; $\Gamma^{\text{replica }(002),\,(110)}{}_L = 0.025°$); ($\sigma^{(004),\,(220)}{}_G = 0.032°$; $\Gamma^{(004),\,(220)}{}_L = 0.032°$; $\sigma^{\text{replica }(004),\,(220)}{}_G = 0.032°$; $\Gamma^{\text{replica}(004),\,(220)}{}_L = 0.032°$). The Δ (°) between the main (002) and (110); (004) and (220) components, as well as

that of their replica is of 0.016°. On the other hand, the shift between the main component (002) and its replica is 0.038°, whereas that of (004), and its replica, is of 0.079°, as expected, and similar to that found for the (111) reflection peak of 0.070° from the bare Si(111) substrate (see Supplementary Fig. S4).

By applying the Bragg's law ($n\cdot\lambda = 2\cdot d\cdot\sin\vartheta$), where $\lambda(Cu\ K_{\alpha 1}) = 1.54056$ Å and n = 1 for the (110), and n = 2 for (002), we get the orthorhombic $CsPbBr_3$ lattice constant values $a_{CsPbBr3} = 8.235$ Å, and $c_{CsPbBr3} = 11.658$ Å, in good agreement with previous literature[15,18,20,21,33–37]. This points to have the type $(002)_{CsPbBr3}$ planes with preferentially aligning parallel to $(111)_{Si}$ planes.

Remarkably, the main peak, containing the (002) and (110) contributions (Fig. 2a) shows a FWHM of 0.06° in the raw profile, which drops down to 0.035° by separating the individual components via fitting. This width is the same order of magnitude as the (111) XRD peak of Si(111) single crystal substrate (0.025°, **Supplementary** Fig. S4). Moreover, the observed value is the lowest reported so far in the literature for orthorhombic $CsPbBr_3$: for instance this is ~ 4.5 times narrower than that reported for a single crystal ingot (0.16°) produced in a two-zone furnace method, and sliced into wafers of 8 mm in diameter and 1.5 mm in thickness[20]. The high intensity of the (002) (110) peaks (Fig. 2) compared to the (111) peak from the Si substrate denotes a preferential film growth along the [001]c perovskite axis. By slightly tilting the sample while keeping the XRD beam and detector conditions unchanged, their intensity is reduced, showing, indeed, a more pronounced Si (111) peak of the substrate (Supplementary Fig. S5). The exceptional characteristics of the XRD data from our $CsPbBr_3$ MBE films indicate a very low density of dislocations or other defects, which, in the literature, often contribute to widen the XRD peak, as well as an absence of residual stress, cushioned by the thin SiO_2 buffer layer.

The high-angle annular dark-field (HAADF) STEM cross-sectional image of a 300 nm $CsPbBr_3$ MBE film grown on SiO_2/Si(111)7 × 7 substrate is reported (Supplementary Fig. S6), while the high-resolution HAADF STEM images of the same film are shown (Fig. 3).

The vertical dashed red line marks the step between two terraces of $CsPbBr_3$ film. It separates two large domains indicated with A, and B, having a lateral size of at least 1 µm. The corresponding HAADF and differential phase contrast (DPC) STEM images aligned to the zone axis are also shown (Fig. 3b) for each domain. They are assigned to the [120] and [010] zone axes of the $CsPbBr_3$. The film was slightly tilted to align onto the zone axis for areas A and B independently. Therefore, the [120], [110] $CsPbBr_3$ and [110] Si planes are not perfectly parallel to each other. The misorientation is as large as a few degrees.

Remarkably, the domains grow sharing the same orientation of the c axis [001], in full agreement with the XRD-defined film texture. The corresponding atomic model of the orthorhombic $CsPbBr_3$ from the given

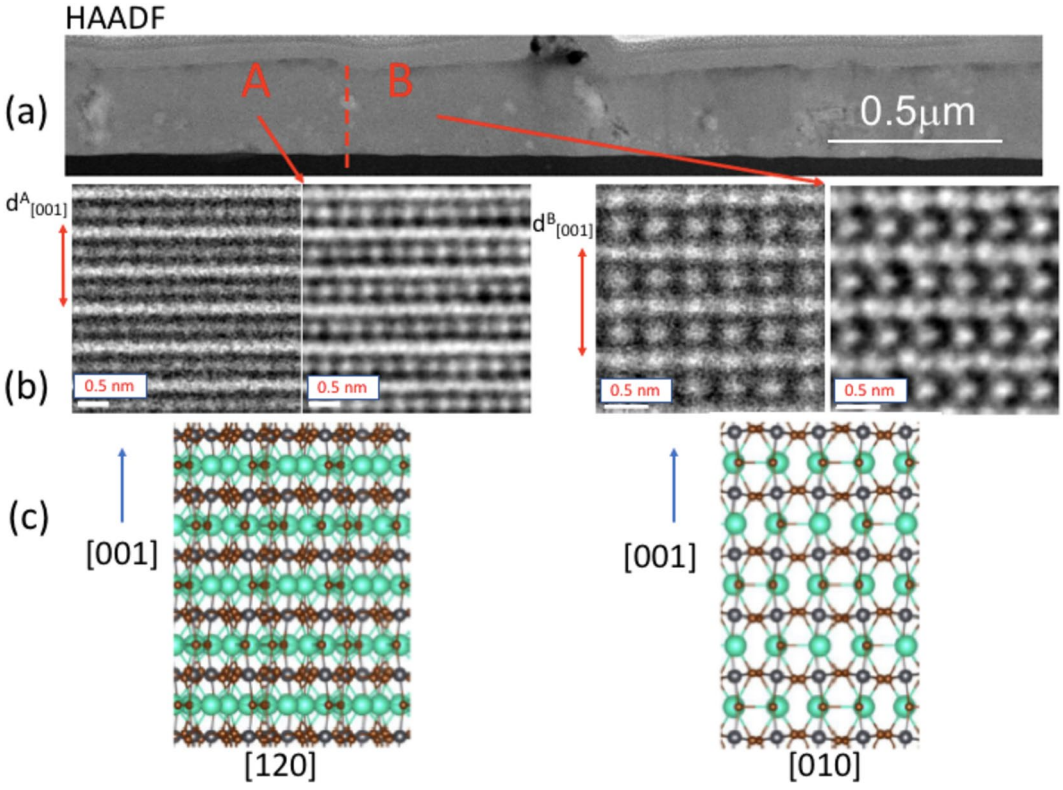

Figure 3. HR HAADF STEM images of 300 nm $CsPbBr_3$ MBE film grown on SiO_2/Si(111)7 × 7: (**a**) HAADF image of the entire cross section; (**b**) atomic resolution HAADF (left) and DPC (right) STEM images of domains A and B tilted to the [120] and [110] zone axes of the $CsPbBr_3$ film respectively; and (**c**) corresponding atomic model for the orthorhombic phase of $CsPbBr_3$ (Cs: light blue, Pb: grey, Br: brown). The vertical dashed red line separates areas A and B.

zone axes are also shown (Fig. 3c). Here, it is worth noting that the distance, $d^{A}_{[001]}$ and $d^{B}_{[001]}$, between the (002) planes (along the [001] direction), is equal to 11.65 Å for both domains, in good agreement with the $c_{CsPbBr3}$ = 11.658 Å found from XRD measurements.

To highlight the overall elemental composition of the $CsPbBr_3$ film, in addition to the HAADF image, the EDX measurements have been performed (Fig. 4). The HAADF cross-section (Fig. 4a) shows the Si substrate (black part, at the bottom), as well as the $CsPbBr_3$ film grown on top (grey). The thin C/Pt protection layer, obtained during the focused ion beam (FIB) preparation of the cross section lamella, is, furthermore, observable at the topmost of the image. We confirm the film thickness estimated by quartz microbalance during the MBE growth, to be about 300 nm. In addition, in some areas on the sample surface, underlined, here, by the two blue circles, some cross-section of parallelogram-like structures, can be recognised, consistent with the surface SEM observations reported below.

The corresponding Pb, Br, and Cs EDX elemental maps of this HAADF image is reported (Fig. 4b, c, d), clearly showing that all three elements are very homogeneously distributed throughout the entire film, exhibiting an average composition of 19 at. % Cs, 19 at. % Pb and 61 at. % Br (with a confidence interval of 1 at %), in good agreement with the stoichiometry of $CsPbBr_3$ perovskite.

To detail better the composition of the entire film, the high-resolution HAADF STEM image of the film cross section tilted to the [110]$CsPbBr_3$ zone axis of area B depicted in Fig. 3, is reported (Fig. 5), including the Si substrate at the bottom (Fig. 5a). Both HAADF image and EDX elemental maps of a similar region at the Si/perovskite interface are also shown (Fig. 5b). An amorphous layer of SiO_2 about 2 nm thick, acting as a buffer layer between the Si substrate and perovskite film, can clearly be observed and identified. A highly ordered homoepitaxial $CsPbBr_3$ film, almost free of defects and/or dislocations, has been obtained. The reasons for the high crystalline quality of this film growth may lie in a multifactorial process.

The presence of the SiO_2 amorphous layer, in conjunction with optimized UHV-MBE growth conditions—specifically the substrate temperature, which primarily affects molecular kinetics, the Knudsen cell, which influences the velocity and flux of CsPbBr3 perovskite molecules and the fact that the stoichiometric $CsPbBr_3$ molecules can arrive intact (Supplementary Information Fig. S3)—has likely facilitated the uniform onset of film growth. This results in a process we term the "*slipping-and- sticking*" mechanism on top of the oxide buffer layer. Consequently, this has promoted the homoepitaxial growth of the $CsPbBr_3$ film to an impressive thickness of 300 nm. Notably, this amorphous thin oxide layer features sharp interfaces on both sides, interfacing with silicon on one side and perovskite on the other, which helps mitigate strain induced by the large lattice parameter mismatch between silicon and $CsPbBr_3$ perovskite.

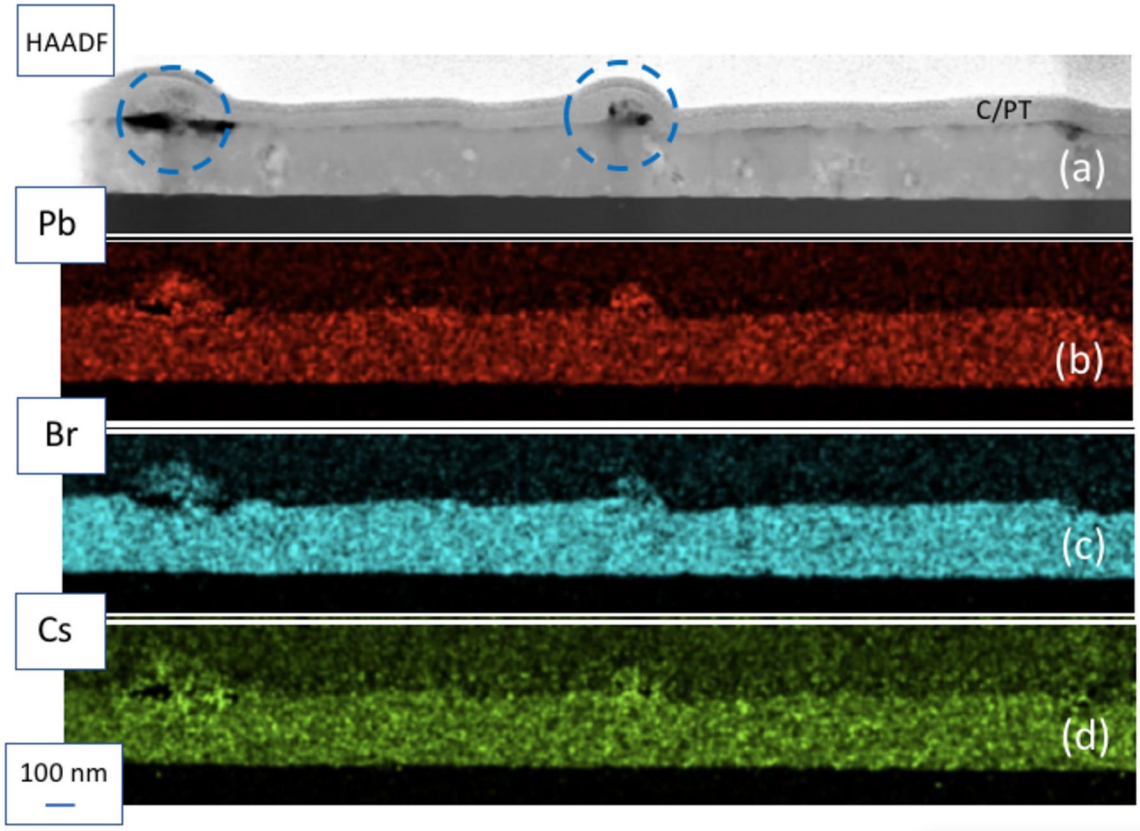

Figure 4. HAADF image (**a**) and Pb (**b**), Br (**c**), and Cs (**d**) EDX elemental maps of 300 nm $CsPbBr_3$ MBE film grown on SiO_2/Si(111)7×7 substrate.

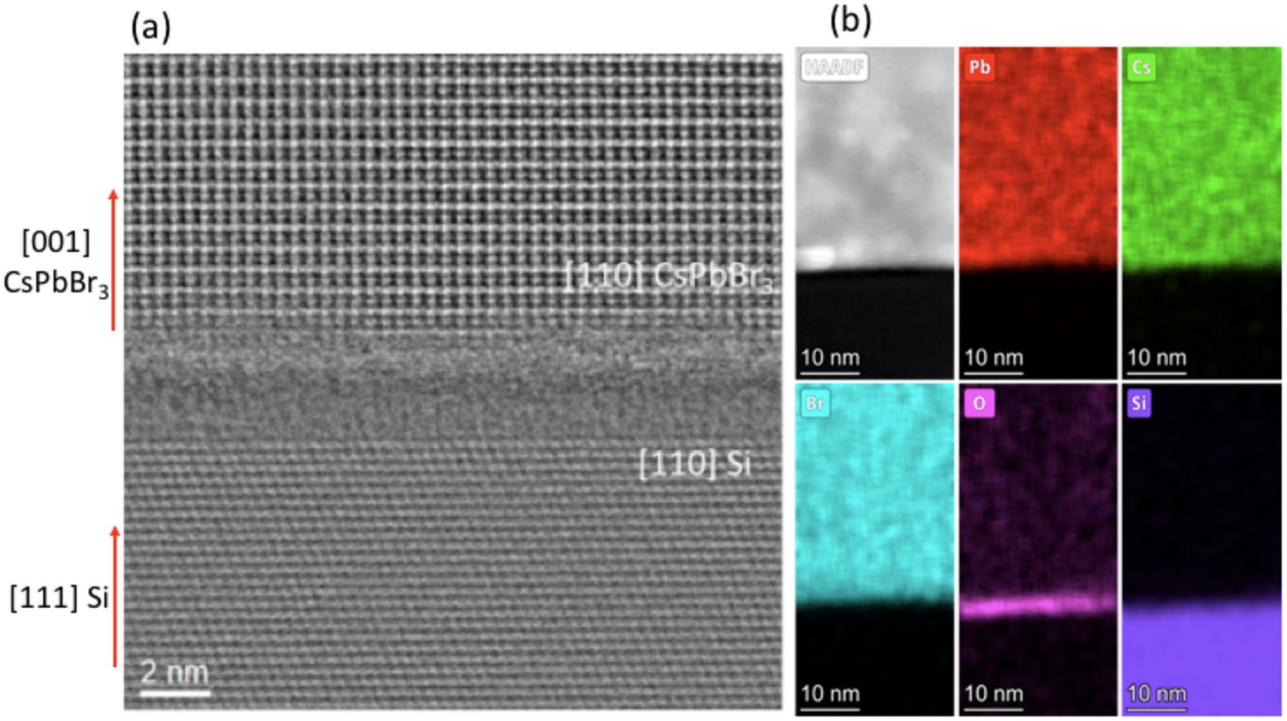

Figure 5. Cross-sectional HAADF-STEM image (**a**) and elemental maps (**b**) of the $CsPbBr_3$ MBE film, including the Si substrate.

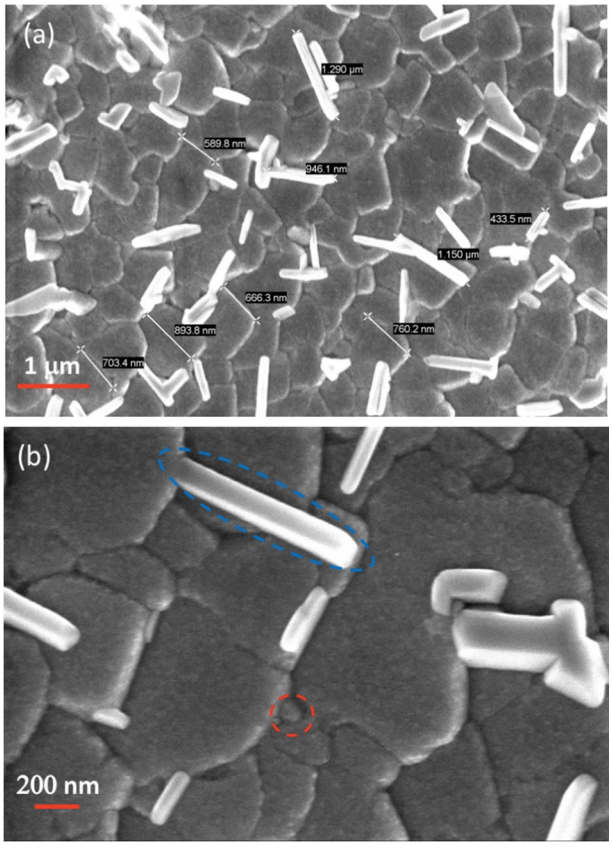

Figure 6. SEM images of the epitaxial $CsPbBr_3$ film. In (**a**) markers indicate the size of terraces and other surface features. In (**b**) the red dashed circle and ellipse mark a small interstitial grain and a 1D structure respectively.

Finally, the surface morphology of the $CsPbBr_3$ film has been investigated by surface SEM measurements. The reported images (Fig. 6) reveal a very compact film, composed by numerous particularly uniform, large and flat terraces. These extended flat terraces have lateral dimensions, ranging between several hundred nanometres and a few microns (Fig. 6a). They arrange in compact interlocking structures, with very narrow gaps. Small grains, like the one surrounded by a red dashed circle (Fig. 6b), are occasionally present but are comparatively rare. It is essential to highlight that this $CsPbBr_3$ structure having obtained by UHV-MBE growth is quite exceptional. Up to now, conventional PLD, and CVD physical methods, have produced epitaxial films composed of much more irregular small grains[29], and separated nanoplates[30].

A second minority morphological phase is present: long and narrow, faceted 1D structures, very bright in the SEM contrast, can be seen on the surface (for example, in the dashed blue ellipse in Fig. 6b), akin to $CsPbBr_3$ nanowires reported in Ref.[41]. They extend for several hundred nanometers in the longitudinal direction and are about 100 nm wide. The same features were visible in cross-section within red dotted circles (Fig. 4a). These nanowires, are only formed on the top surface of the film and do not affect the bulk properties of the material underneath. They represent a minority, and could be explained by the presence of a residual vacuum dominated by the perovskite, persisting for a few hours, even after the closing of the Knudsen shutter cell. They could be avoided placing, directly, a capping layer of other possible/useful materials, just after the film growth.

In summary, we reported the growth of thin (~ 10 nm) and thick (~ 300 nm) $CsPbBr_3$ perovskite, by UHV-MBE, on Si(111)7 × 7 and SiO_2/Si(111)7 × 7, after *in-situ* formation of a thin oxide layer, introduced as a buffer layer to decouple the Si substrate from the perovskite film. The growth of $CsPbBr_3$ showed a RHEED pattern with × 2 surface reconstruction. Ordered thick films (up to 300 nm) of $CsPbBr_3$ with orthorhombic *Pbmn* (62) structure were achieved on SiO_2/Si(111)7 × 7, as attested by XRD, HAADF STEM, EDX, and SEM measurements, thanks to a *slipping-and-sticking* process induced by the thin amorphous SiO_2 layer. The excellent crystal quality of the film was proven by the narrowest reported FWHM of the (002) and (110) XRD reflections (0.035°), comparable to that of Si(111) substrate (Supplementary Information Fig. S4), in addition, the electron microscopy studies also demonstrated the presence of micron-scale single crystal terraces. It is noteworthy that the results presented in this work are a significant advancement in the study and development of materials, crucial for optoelectronic and energy conversion applications. Specifically, halide perovskites such as $CsPbBr_3$, synthesized from entirely inorganic precursor salts under ultra-high vacuum conditions, pave the way for the creation of new nanostructures with exceptional fundamental physical properties.

Methods

In-situ experiments were performed at the CNR-ISM laboratory of Tor Vergata, Rome (Italy). The Si(111) substrates were cleaned in a UHV MBE chamber (base pressure: 8.0×10^{-10} mbar) by applying several flashes, at about 1150 °C, until the Si(111)7 × 7 reflection high electron energy diffraction (RHEED) pattern of clean silicon was obtained. Molecular deposition of $CsPbBr_3$ was carried out, keeping the substrate at 130 °C. The mass spectrometry was carried out by SRS RGA-300 AMU, during the $CsPbBr_3$ films growth. AES spectra were collected at the normal incidence with a primary electron beam of EP = 3.0 keV. AES data were acquired in the first derivative mode with a PHY 255G double-pass cylindrical mirror analyser equipped with a coaxial electron gun, with a resolution of 0.5 eV. The Si(111)7 × 7 surface was exposed to 1.2×10^4 Langmuir (L) (1 L = 1×10^{-6} mbar · 1 s) of O_2 at RT in order to oxidise the first few nm into amorphous SiO_2. Thin (~ 10 nm) and thick (~ 300 nm) $CsPbBr_3$ were evaporated on clean Si(111)7 × 7 surface, and after exposure to O_2. The substrate was kept at ~ 130 °C during MBE growth with a rate of ~ 0.1 Å/s from a Knudsen cell (RIBER) loaded with stoichiometric $CsPbBr_3$ powder, purchased from TCI CAS RN :15243-48-0, with low water content, without any further purification. (A thin film of native silicon(111) is also suitable for growth of $CsPbBr_3$).

Ex-situ X-ray diffraction (XRD) measurements were performed at University of Roma 2, Engineering Dep., Rome (Italy) by means of a Rigaku SmartLab diffractometer, working in ((ϑ—2ϑ) Bragg–Brentano geometry, equipped with a Cu source ($K\alpha_1$ = 1.54056 Å, $K\alpha_2$ = 1.54439 Å) and a D/teX Ultra 250 silicon strips detector. XRD spectra (5°- 60°) were acquired in a single scan with a step of 0.05°, ~ 0.2 s/pt, and a horizontal slit of 5 mm. Scanning electron microscopy (SEM) measurements were performed by using a ZEISS SIGMA 300 FESEM.

High-resolution scanning transmission electron microscopy (STEM) characterisation was performed in a double corrected ThermoFisher Spectra 300 S/TEM operated at 300 kV. Images were acquired using a current of 50 pA. Segmented STEM detectors allow the acquisition of both High-Angle Annular Dark Field (HAADF) and Differential Phase Contrast (DPC) images. Compositional maps were acquired using Velox, with a probe current of ~ 150 pA and rapid raster scanning, collecting the Energy-Dispersive X-Ray (EDX) signal on a Dual-X system comprising two detectors on either side of the sample, for a total acquisition angle of 1.76 Sr. A cross-section of the films with a final thickness of 150 nm was prepared by Focused Ion Beam (FIB) milling using a Helios Nanolab FIB/SEM (Thermo Fisher Scientific). A thin layer of platinum (200 nm) was deposited over the target area of the film using the electron beam (2 nA, 5 kV) prior exposure to the ion-beam. A standard in-situ lift-out procedure was employed. Further thinning was performed at 30 kV/100 pA. Final polishing was at a reduced voltage of 2 kV. This procedure minimizes the amount of damaged material on the surface and reduces the levels of implanted gallium in the final thin foil.

Data availability

All data generated or analysed during this study are included in this published article [and its supplementary information files].

Received: 4 April 2024; Accepted: 17 July 2024
Published online: 09 October 2024

References

1. Rose, G. Beschreibung einiger neuen Mineralien des Urals. *Poggendorffs Ann. Phys. Chem.* **124**, 551–573 (1839).
2. Katz, E. A. Perovskite: Name puzzle and german-russian odyssey of discovery. *Helv. Chim. Acta* **103**, e200006–e200011 (2020).
3. Megaw, H. Crystal structure of barium titanate. *Nature* **155**, 484–485 (1945).
4. Rooksby, H. P. Compounds of the structure type of the calcium titanate. *Nature* **155**, 484 (1945).
5. Yashima, M. & Ali, M. Structural phase transition and octahedral tilting in the calcium titanate perovskite $CaTiO_3$. *Solid State Ionics* **180**, 120–126 (2009).
6. Shi, F., Fu, G., Xiao, E.-C. & Li, J. Lattice vibrational characteristics and dielectric properties of pure phase $CaTiO_3$ ceramic. *J. Mater Sci. Mater Electron.* **31**, 18070–18076 (2020).
7. Kojima, A., Teshima, K., Shirai, Y. & Miyasaka, T. Organometal halide perovskites as visible-light sensitizers for photovoltaic cells. *J. Am. Chem. Soc.* **131**, 6050–6051 (2009).
8. Lee, M. M., Teuscher, J., Miyasaka, T., Murakami, T. N. & Snaith, H. J. Efficient hybrid solar cells based on meso-superstructured organometal halide perovskites. *Science* **338**, 643–647 (2012).
9. Jena, A. K., Kulkarni, A. & Miyasaka, T. Halide perovskite photovoltaics: Background, status, and future prospects. *Chem. Rev.* **119**, 3036–3103 (2019).
10. Iso, Y. & Isobe, T. Review: Synthesis, luminescent properties, and stabilities of cesium lead halide perovskite nanocrystals. *ECS J. Solid State Sci. Technol.* **7**, R3040–R3045 (2018).
11. Pan, Y. *et al.* Progress in the preparation and application of $CsPbX_3$ perovskites. *Mater. Adv.* **3**, 4053–4068 (2022).
12. Liu, X., Li, J., Wang, X. & Yang, D. Inorganic lead-based halide perovskites: From fundamental properties to photovoltaic applications. *Mater. Today* **61**, 191–217 (2022).
13. Wang, K. *et al.* Progress of inverted inorganic cesium lead halide perovskite solar cells. *Cell Rep. Phys. Sci.* https://doi.org/10.1016/j.xcrp.2023.101726 (2023).
14. Guo, W. *et al.* Stability of hybrid organic-inorganic perovskite $CH_3NH_3PbBr_3$ nanocrystals under Co-stresses of UV light illumination and temperature. *Nanomaterials* **9**, 1158. https://doi.org/10.3390/nano9081158 (2019).
15. Zhang, C. *et al.* Thermal stability of $CsPbBr_3$ perovskite as revealed by in situ transmission electron microscopy. *APL Mater.* **7**, 071110–071116 (2019).
16. Kanak, A. *et al.* Melting and crystallization features of $CsPbBr_3$ perovskite. *Cryst. Growth Des.* **22**, 4115–4121 (2022).
17. Moller, C. K. Crystal structure and photoconductivity of caesium plumbohalides. *Nature* **182**, 1436 (1958).
18. Stoumpos, C. C. Crystal growth of the perovskite semiconductor $CsPbBr_3$: A new material for high-energy radiation detection. *Cryst. Growth Des.* **13**, 2722–2727 (2013).
19. Hirotsu, S., Harada, J., Iizumi, M. & Gesi, K. Structural phase transition in $CsPbBr_3$. *J. Phys. Soc. Jpn.* **37**, 1393–1398 (1974).
20. Zhang, M. *et al.* Growth and characterization of all-inorganic lead halide perovskite semiconductor $CsPbBr_3$ single crystals. *Cryst. Eng. Comm.* **19**, 6797–6803 (2017).
21. Cottingham, P. & Brutchey, R. L. On the crystal structure of colloidally prepared $CsPbBr_3$ quantum dots. *Chem. Commun.* **52**, 5246–5249 (2016).
22. Zhang, D., Eaton, S. W., Yu, Y., Dou, L. & Yang, P. Solution-phase synthesis of cesium lead halide perovskite nanowires. *J. Am. Chem. Soc.* **137**, 9230–9923 (2015).
23. Protesescu, L. *et al.* Nanocrystals of cesium lead halide perovskites (CsPbX3, X = Cl, Br, and I): Novel optoelectronic materials showing bright emission with wide color gamut. *Nano Lett.* **15**, 3692–4369 (2015).
24. Swarnkar, A. *et al.* Colloidal $CsPbBr_3$ perovskite nanocrystals: Luminescence beyond traditional quantum dots. *Angew. Chem. Int. Ed.* **54**, 15424–15428 (2015).
25. Tian, C. *et al.* Chemical vapor deposition method grown all-inorganic perovskite microcrystals for self-powered photodetectors. *ACS Appl. Mater. Interfaces.* **11**, 15804–15812 (2019).
26. Bonomi, S. & Malavasi, L. Physical and chemical vapor deposition method supplied to all-inorganic metal halide perovskites. *J. Vac. Sci. Tech. A.* **38**, 060803–060811 (2020).
27. Dey, A. *et al.* State of the art and prospects for halide perovskite nanocrystals. *ACS Nano* **15**, 10775–10981 (2021).
28. Wang, L., King, I., Chen, P., Bates, M. & Lunt, R. R. Epitaxial and quasiepitaxial growth of halide perovskites: New routes to high end optoelectronics. *APL Mater.* **8**, 100904–22 (2020).
29. Yuan, B. *et al.* Epitaxial growth of quasi-intrinsic $CsPbBr_3$ film on a $SrTiO_3$ substrate by pulsed laser deposition. *ACS Appl. Electron. Mater.* **3**, 5592–5600 (2021).
30. Chen, J. *et al.* Single-crystal thin films of cesium lead bromide perovskite epitaxially grown on metal oxide perovskite ($SrTiO_3$). *J. Am. Chem. Soc.* **139**, 13525–13532 (2017).
31. Zhang, Y. *et al.* Preparation of $CsPbBr_3$ films with tens of micrometer-scale grains and preferential orientation for perovskite solar cells. *ACS Appl. Energy Mater.* **6**, 12190–12197. https://doi.org/10.1021/acsaem.3c01133 (2023).
32. Rieger, J. *et al.* Epitaxial inorganic metal-halide perovskite films with controlled surface terminations. *Phys. Rev. Mat.* **7**, 035403–035406 (2023).
33. Hooper, T. J. N., Fang, Y., Brown, A. A. M., Pu, S. H. & White, T. J. Structure and surface properties of size-tuneable $CsPbBr_3$ nanocrystals. *Nanoscale* **13**, 15770–15789 (2021).
34. Imran, M. *et al.* Colloidal synthesis of strongly fluorescent $cspbbr_3$ nanowires with width tunable down to the quantum confinement regime. *Chem. Mater.* **28**, 6450–6454 (2016).
35. López, C. A. *et al.* Crystal structure features of $CsPbBr_3$ perovskite prepared by mechanochemical synthesis. *ACS Omega* **5**, 5931–5938 (2020).
36. Bertolotti, F. *et al.* Coherent nanotwins and dynamic disorder in cesium lead halide perovskite nanocrystals. *ACSNano* **11**, 3819–3831 (2017).
37. Toso, S., Baranov, D., Giannini, C., Marras, S. & Manna, L. Wide-Angle X-ray diffraction evidence of structural coherence in $CsPbBr_3$ nanocrystal superlattices. *ACS Mater. Lett.* **1**, 272–276 (2019).
38. Ahmad, Z. & Mishra, A. Growth of $PbBr_2$ microrods with unique structure and surface morphology. *J. Mater. Sci. Mat. Electr.* **31**, 4672–4676 (2020).
39. De Padova, P. *et al.* Identification of the Si 2p Surface Core Level Shifts on the Sb/Si(001)-2 × 1 Interface. *Phys. Rev. Lett.* **81**, 2320–2323 (1998).
40. Larciprete. R., De Padova, P. *et al.* Ge/Si(001)c(4 × 2) interface formation studied by high-resolution Ge 3d and Si 2p core-level spectroscopy. *Phys. Rev B.* **61**, 16006–16014 (2000).
41. Eaton, S. W. *et al.* Lasing in robust cesium lead halide perovskite nanowires. *PNAS* **113**, 1993–1998 (2016).

Acknowledgements

This work was supported by the EU Horizon 2020 Framework Programme Call: H2020-LC-SC3-2020-RES-RIA CitySolar Project grant N: 101007084. A. D. C. acknowledges CANVAS project of Ministero della Transizione Ecologica – Ricerca di Sistema (CUP B53C22009710005), Cinzia Giannini, director of Institute of Crystallography of CNR, is recognized for the fruitful scientific discussion, mainly related to the XRD measurements. The

authors are grateful to L. Imperatori, S. Priori, and A. Ippoliti for their invaluable technical support. Y. P. I. and G. D. thank Dr. Paola Parlanti and Dr. Mauro Gemmi for access to the FIB in CMI@SSSA.

Author contributions

P. D. P. and A. D. C. conceived the idea of this project. P. D. P., C. O. and B. O. grown $CsPbBr_3$ films in the UHV MBE apparatus; cleaned the Si(111)7 × 7 substrates and performed the thin SiO_2 layers on Si(111)7 × 7 substrates. P. D. P., C. O. and B. O. carried out the RHEED patterns, Auger electron spectroscopy and relative data analysis. P. D. P. performed the XRD, SEM and PL measurements and relative data analysis. Y. P. I. and G. D. carried out the STEM characterization and relative data analysis. P. D. P. wrote the original draft. C. O., B. O., I. Y., G. D. and A. D. C. helped to edit and review the manuscript. A. D. C. secured funding. All authors contributed to the discussion of results and the final manuscript preparation.

Competing interests

The authors declare no competing interests.

Additional information

Supplementary Information The online version contains supplementary material available at https://doi.org/10.1038/s41598-024-67889-8.

Correspondence and requests for materials should be addressed to P.P., G.D. or A.C.